Available online at www.sciencedirect.com
ScienceDirect
Ceramics International 35 (2009) 1501–1508
CERAMICS INTERNATIONAL
www.elsevier.com/locate/ceramint

The reaction between the magnesia–chrome brick and the molten slag of $MgO–Al_2O_3–SiO_2–CaO–Fe_tO$ and the resulting microstructure

Moo-Chin Wang [a], Chia-Chan Hsu [b], Min-Hsiung Hon [b,*]

[a] Department of Fragrance and Cosmetic Science, Kaohsiung Medical University, 100 Shih-Chuan 1 st Road, Kaohsiung 80728, Taiwan
[b] Department of Materials Science and Engineering, National Cheng Kung University, 1 Ta-Hsueh Road, Tainan 70101, Taiwan

Received 28 May 2008; received in revised form 20 June 2008; accepted 6 August 2008
Available online 9 September 2008

Abstract

The reaction and microstructure at the interface of $MgO–Cr_2O_3$ brick and the molten slag of $MgO–Al_2O_3–SiO_2–CaO–Fe_tO$ after static slag corrosion at 1823–1923 K for various times and the resulting microstructure were investigated and characterized. After the static slag corrosion at 1923 K for 4 h, the XRD results show the major phases of periclase MgO, $MgCr_2O_4$ spinel, and $CaMgSiO_4$ as the minor phase. $MgCr_2O_4$ phase causes MgO to form a discontinuous phase in $MgO–Cr_2O_4$ brick. After static slag corrosion at 1923 K for 4 h, SEM micrographs show that brick interior cracks, MgO and dissolved MgO. MgO dissolved due to the molten plag penetrated into the brick interior and reaction with it, leading to a localized dissolution of brick slag. TEM micrographs and ED patterns demonstrate that the minor phase of $(Mg, Fe)(Al, Cr)_2O_4$ precipitates in the $MgCr_2O_4$ matrix.

Keywords: B. Optical microscopy; B. X-ray methods; C. Chemical properties; D. Glass ceramics; D. Al_2O_3

1. Introduction

The direct iron ore smelting (DIOS) reduction process and an environmentally oriented steel making process are the subjects of the present research. The DIOS process eliminates the need for a coke oven and a sintering plant. Although the DIOS process has many advantages, there are several limiting factors to productivity, including controllable factors such as carbonaceous material in slag, slag volume, and hot metal temperature. The reduction rate of the DIOS process depends on the overall apparent rate constant and the FeO content of the foamy slag. For a good productivity, it is necessary to satisfy the reduction rate and thermal state concurrently within controlled hot metal temperature condition [1]. Hence, selecting suitable refractories for use in a DIOS furnace environment is very important.

Keith [2] pointed out that there are no ternary compounds at liquids temperatures in the system $MgO–Cr_2O_3–SiO_2$. Glasser and Osborn [3,4] published a phase diagram of the system $CaO–Cr_2O_3–SiO_2$, which shows relationships at liquids temperatures for all but the high-line part of the system. Morita et al. [5] determined the solubilities of chromite in $MgO–Al_2O_3–SiO_2–CaO$ melts in air. They found that the solubility of picrochromite increased from 0.2–0.8 wt% Cr_2O_3 to 0.5–2.6 wt% Cr_2O_3 by adding CaO (wt% CaO/wt% SiO_2 = 1) to the $MaO–Al_2O_3–SiO_2$ melts. For Al_2O_3 containing melts, the chromium in the chromite $MgO–Cr_2O_3$ was substituted by aluminum in proportion to Al_2O_3 content in the melt. The amount of secondary spinal have a correlation with the hot strength and corrosion resistance of the magnesia–chrome ($MgO–Cr_2O_3$) bricks, which are largely affected by firing temperature and raw material combination, as reported by Ichikawa et al. [6] $MgO–Cr_2O_3$ bricks have been widely used in the steel refining process and they are also considered as potential materials for a DIOS furnace [7]. The corrosion of $MgO–Cr_2O_3$ bricks with molten $CaO–SiO_2–Al_2O_3–Fe_tO–MgO$ (where Fe_tO denotes the total iron concentration) at 1773 K in an Ar atmosphere has been illustrated by Tao et al. [8], revealing that the main corrosion modes of $MgO–Cr_2O_3$ bricks with molten slag in a static condition are the local corrosion at the slag surface and the pit-like

* Corresponding author. Tel.: +886 6 2757575x62932; fax: +886 6 2380208.
E-mail address: mhhon@mail.ncku.edu (M.-H. Hon).

0272-8842/$34.00 © 2008 Published by Elsevier Ltd and Techna Group S.r.l.
doi:10.1016/j.ceramint.2008.08.008

corrosion at the bottom surface of the bricks in the bulk slag phase and in the upper part of a local corrosion zone. Moreover, Tao et al. [9] also demonstrated the main corrosion mode of MgO–Cr_2O_3 bricks by molten CaO–SiO_2–Al_2O_3–Fe_tO slag and metal at 1873 K in static conditions of an Ar atmosphere in the local corrosion at the slag–metal interface. However, an extensive literature search shows that the details of the reaction between the MgO–Cr_2O_3 bricks and the molten slag of MgO–Al_2O_3–SiO_2–CaO–Fe_tO and the resulting microstructure have not been clarified.

Although the MgO–Cr_2O_3 brick has been used in the DIOS process, the attack of bricks is a complex phenomenon involving chemical (corrosion) and a physical/mechanical (erosion and abrasion) processes as well as thermal shock and spalling. As in any chemical reaction between a solid body and a liquid, corrosion of bricks by molten liquids involves reactant contact to enable the reaction to take place, and product transport to allow it to proceed [10]. Furthermore, convercial MgO–Cr_2O_3 bricks have a heterogeneous microstructure, consisting of multiple components including many pores. Tao et al. [9] have also demonstrated that the dissolution of MgO–Cr_2O_3 bricks causes not only the compositional gradient in the slag phase but also an oxygen concentration gradient in the metal phase at the slag–metal interface. Hence, a studying of the corrosion between the MgO–Cr_2O_3 brick and the molten slag in air is expected to provide primary information for establishing a reliable method for evaluating corrosion resistance and for developing more corrosion-resistant refractory bricks.

In this study, the reaction between MgO–Cr_2O_3 brick and the molten slag of MgO–Al_2O_3–SiO_2–CaO–Fe_tO using electric furnace static slag corrosion and the resulting microstructure were investigated. Examination conditions are 1823–1923 K, oxidizing atmosphere, low slag basicity (Ca/Si = 1.1), and slag containing Fe_tO 5.0 wt%.

2. Experimental procedure

The starting slag used in an oxidizing atmosphere at 1823–1923 K was a synthetic system based on MgO–Al_2O_3–SiO_2–CaO–Fe_tO with commercial reagents of MgO, Al_2O_3, SiO_2, and $CaCO_3$. The chemical composition of these oxide powders is listed in Table 1. The MgO–Al_2O_3–SiO_2–CaO premelted slag was fused in an Al_2O_3 crucible at 1823 K in air for 2 h, then quenched in water, dried, and ground in a steel mortar. Subsequently, the ground-premelted slag was mixed with FeO to make the described composition for experiments. The compositions of FeO and Fe_2O_3, and Fe_tO in the experimental slag are listed in Tables 2 and 3, respectively.

The specimens for the immersion test (60 mm × 60 mm × 60 mm) were obtained from commercial MgO–Cr_2O_3 bricks. The chemical composition and properties of the MgO–Cr_2O_3 bricks are listed in Table 4. The crucible (13.2 cm inside diameter, 15.0 cm outside diameter, and 12.0 cm depth) for the electric furnace static slag corrosion test was fabricated with castable refractories. An inner fused-alumina crucible (Al_2O_3 99.5%) with a 11.2-cm inside diameter, a 13.0-cm outside diameter, and a 10.0-cm depth containing 300 g of slag and the sample, was set in the castable crucible.

The schematic diagram of the experimental electric furnace and crucibles used for the static slag corrosion test is shown in Fig. 1, with water-cooled cap-sealing upper and lower ends of the steel chamber. The furnace temperature was controlled by a 20% Rh/Pt–40% Rh/Pt thermocouple connected to a proportional-integral-derivative (PID) program controller and listed in Table 5.

The castable crucible contained an Al_2O_3 crucible and slag. The sample was put in the furnace and heated in air. The crucible was held at 1823–1923 K for 2–8 h. After a corrosion test for a specified time, the MgO–Cr_2O_3 brick specimen was removed from the slag by lowering the crucible. The specimen

Table 1
Chemical composition of oxide powders.

Oxide powders	Composition (wt%)							
	SiO_2	Al_2O_3	CaO	MgO	Fe	Pb	SO_4	Others
SiO_2[a]	98.92			0	0.01	0.01	0.05	1.01
Al_2O_3[b]		98.50	0	0	0.02			1.3
$CaCO_3$[c]			55.20		0.01	0.001		44.739
MgO[d]				>98.00	0.03	0.02		1.85

[a] Nacalai Tesque, INC., Kyoto, Japan.
[b] J. T. Back, USA.
[c] Yakuri Chem. Co., Ltd. Osaka, Japan.
[d] Yakuri Chem. Co., Ltd. Osaka, Japan.

Table 2
Source and composition of FeO.

Source	Composition (wt%)					
	SiO_2	Al_2O_3	CaO	MgO	FeO	Fe_2O_3
China Steel Corporation	0.21	0.19	0.08	0.02	69.50	30.00

Table 3
Chemical composition of the slag.

Composition (wt%)					C/S[a]
MgO	Al_2O_3	SiO_2	CaO	Fe_tO[b]	
12.0	15.0	32.4	35.6	5.0	1.1

[a] $C/S = CaO/SiO_2$.
[b] Fe_tO contained FeO 69.50 wt% and Fe_2O_3 30.00 wt%.

was vertically sectioned at the center for a visual inspection of corrosion and slag penetration.

The crystalline phases of the MgO–Cr_2O_3 brick were identified by a Rigaku X-ray diffractometer (XRD Model Rad IIA, Rigaku Co., Tokyo, Japan) with Cu radiation and a Ni filter at a scanning rate (2θ) of 0.25° min^{-1}.

The sample for optical polarized microscopy (OPM, Model Nikon E600POL, Japan) was prepared as follows: the sample was sliced from the brick with an ultrasonic cutter, mechanically ground to a thickness of about 80 μm, and then polished to optical transparency with diamond pastes.

The morphology of the corroded surface and permeated layer of the MgO–Cr_2O_3 brick before and after slag corrosion was examined using scanning electron microscopy (SEM, Model S-4200, Hitachi Ltd., Tokyo, Japan). The composition was analyzed using energy dispersive spectrometric (EDS) (Model Noran, USA) mapping and line scanning attached to SEM (S-4200).

The foil for transmission electron microscopy (TEM, Model JEOL 3013, JOEL Ltd., Tokyo, Japan) was prepared using the conventional technique: the sample was taken to the optical thin foil machined and ion-beam thinned to electron transparency. Electron diffraction (ED) examination was made at an accelerating voltage of 200 kV on the carefully thinned foils of the MgO–Cr_2O_3 brick after the slag corrosion test.

Table 4
Composition and physical properties of the MgO–Cr_2O_3 brick* for slag corrosion test.

Refractory	Composition (wt%)				Physical properties		
	Al_2O_3	MgO	Fe_2O_3	Cr_2O_3	B.D.[a] (g/cm^3)	A.P.[b] (%)	C.C.S.[c] (MPa)
MgO–Cr_2O_3	5.0	53.2	7.3	34.5	3.3	15.3	33

* Provided by supplier (Kuan-Ho DIS-1).
[a] B.D.: bulk density.
[b] A.P.: apparent porosity.
[c] C.C.S.: cold crush strength.

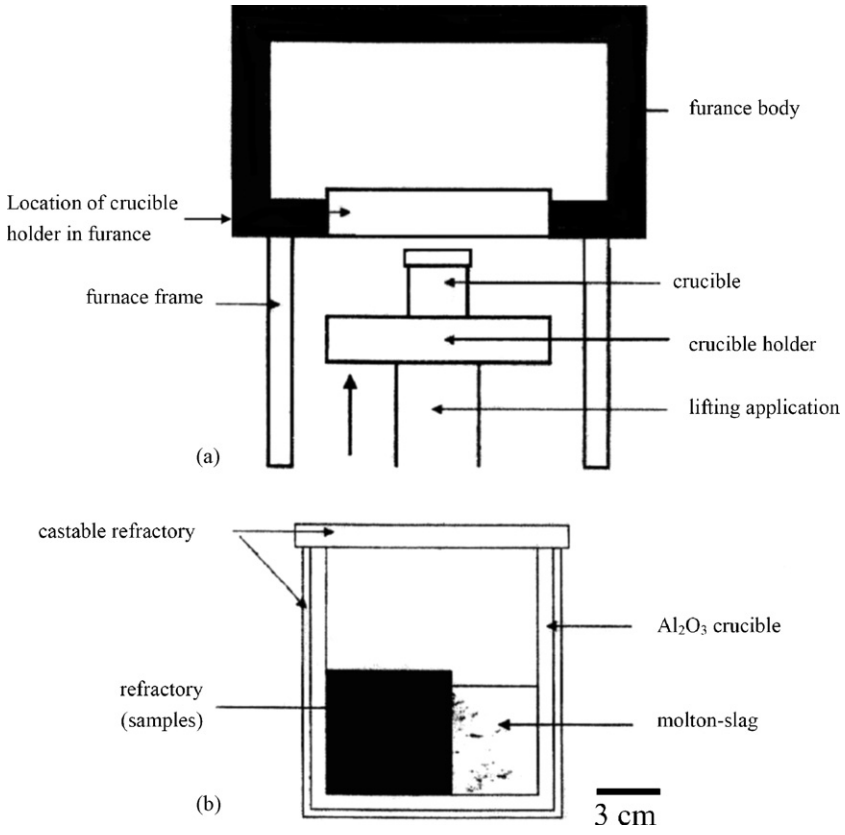

Fig. 1. The schematic diagrams of (a) experimental electric furnace and (b) crucible for the static slag corrosion test.

Table 5
Chemical composition of the slag after the electric furnace static slag corrosion test.

Test condition (K/h)	Composition (wt%)				
	MgO	CaO	SiO_2	Al_2O_3	Fe_tO
1823/2	14.8	32.7	31.0	14.0	7.5
1823/4	15.3	32.5	31.3	13.6	7.3
1823/6	16.7	32.3	30.4	13.5	7.1
1823/8	18.6	31.5	29.4	13.3	7.2
1873/2	16.7	31.4	31.2	13.5	7.2
1873/4	18.6	31.4	29.5	13.3	7.2
1873/6	21.6	30.1	28.7	12.6	7.0
1873/8	23.0	30.0	28.6	11.6	6.8
1923/2	23.6	30.4	27.9	11.5	6.6
1923/4	26.0	29.2	27.1	11.6	6.1
1923/6	27.0	28.7	26.8	11.6	5.9
1923/8	28.3	28.5	26.2	11.2	5.8

3. Results and discussion

3.1. Morphology and phases of the $MgO–Cr_2O_3$ bricks before and after the corrosion test

Fig. 2 shows the SEM micrographs of the $MgO–Cr_2O_3$ brick before the slag corrosion test $MgCr_2O_4$, MgO pores and cracks

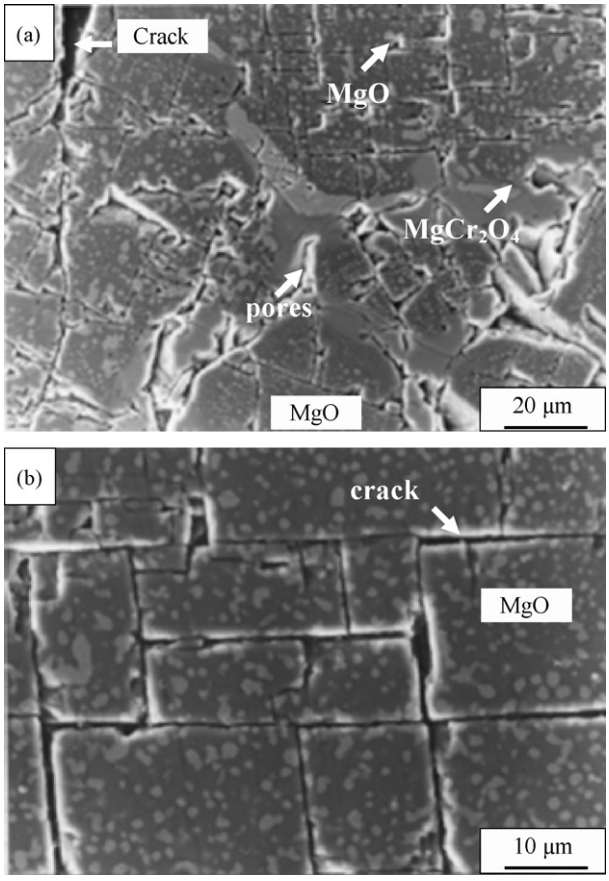

Fig. 2. SEM morphology of $MgO–Cr_2O_3$ brick before the test: (a) MgO, $MgCr_2O_3$, pores, and cracks, and (b) enlarged view of MgO periclase in (a).

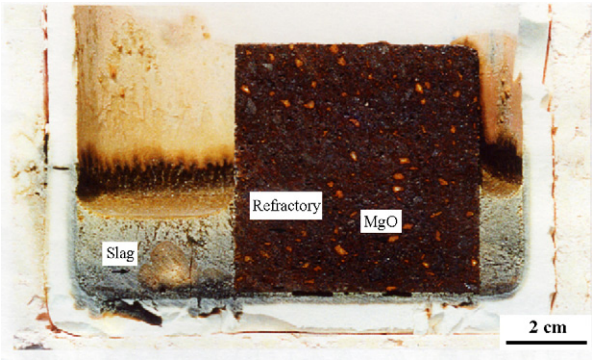

Fig. 3. The cross-section morphology of $MgO–Cr_2O_3$ brick reacted with molten slag of $MgO–Al_2O_3–SiO_2–CaO–Fe_tO$ after the static corrosion test at 1923 K for 2 h.

are in the $MgO–Cr_2O_3$ brick interior has been identified in Fig. 2(a). The crystal contain substantial closed porosity because of the large grain growth, leaving pores in the center of grains where volume diffusion is slow. The bonding second phase of pores and cracks with in a sintered aggregate particle in a refractory microstructure is a source of weakness because it is susceptible to slag penetration into the $MgO–Cr_2O_3$ brick interior and caused a corrosion reaction between the $MgO–Cr_2O_3$ brick and molten slag.

Fig. 2(b) shows the enlarged view of MgO area in Fig. 2(a). The cracks around the MgO formed an area of continuous phase of periclase in the $MgO–Cr_2O_3$ bricks. Most MgO is in a periclase form, which is difficult to dislodge by corrosion. In contact with molten iron and slag, the MgO is modified by reaction with oxides. Hence, the periclase MgO in the $MgO–Cr_2O_3$ brick with which the high-temperature refracting properties are used against the aggressive environment [11].

Fig. 3 shows the cross-section micrograph of the $MgO–Cr_2O_3$ brick with reacted the molten slag of $MgO–Al_2O_3–SiO_2–$

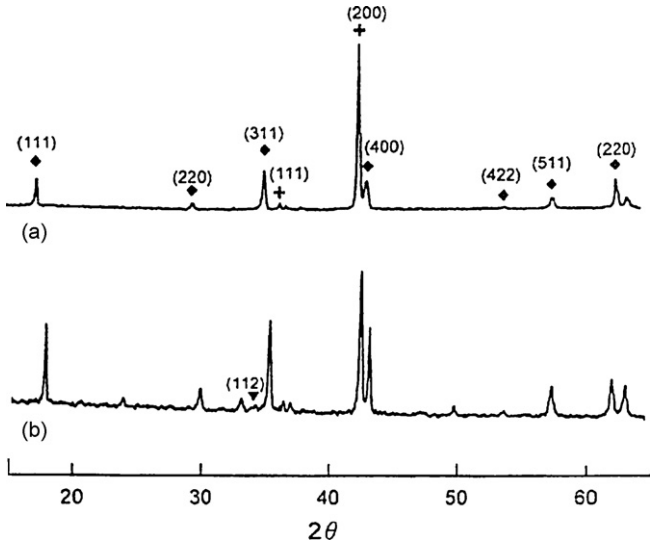

Fig. 4. XRD patterns of $MgO–Cr_2O_3$ brick (a) before the test, and (b) test at 1923 K for 4 h. +: MgO, ◆: $MgCr_2O_4$ ▼: $CaMgSiO_4$.

CaO–Fe_tO at 1873 K for 2 h. There is no significant corrosion at the interface of MgO–Cr_2O_3 brick and slag. Fig. 3 also indicates that after the test, the slag content decreased, which is partly caused by the slag reaction with the Al_2O_3 crucible, and MgO–Cr_2O_3 brick, and partly by slag penetration into MgO–Cr_2O_3 brick. The dimensions of MgO–Cr_2O_3 bricks remained near 60 mm × 60 mm × 60 mm after the corrosion test at 1923 K for 8 h. The interface of the MgO–Cr_2O_3 brick and the molten slag was still smooth. No obvious corrosion evidence was identified after the test at 1923 K for 8 h. Moreover, the MgO–Cr_2O_3 brick had about 15.37% apparent porosity, which provides the channel for slag attack. Evaluation of the slag attack can be make by the width of the reaction product layer of the slag with brick. The width of the reaction product layer for the molten slag and is only about 0.5 μm after a corrosion test at 1823 K for 2 h. The width of reaction product layer increases with test temperature and time. After a test at 1923 K for 8 h, the width approached 2.0 μm.

Fig. 4 shows the XRD patterns of the MgO–Cr_2O_3 brick before and after a test at 1923 K for 4 h. Before the test, the crystalline phases of MgO–Cr_2O_3 brick are MgO periclase and $MgCr_2O_4$ spinel, as shown in Fig. 4(a). After a test at 1923 K for 4 h, the diffraction peaks of MgO and $MgCr_2O_4$ successively appear and the minor crystalline phase, $CaMgSiO_4$, also shows up, as shown in Fig. 4(b).

Fig. 5 illustrates the open Nicol of an optical polarized microscopy (OPM) of MgO–Cr_2O_3 brick with molten slag of MgO–Al_2O_3–SiO_2–CaO–Fe_tO at 1923 K for 8 h. Using the extinction and relief of OPM, the crack, pores, MgO, $MgCr_2O_4$, and corrosion reaction area has been identified. Fig. 5 indicates that there are cracks and pores in the interior of MgO–Cr_2O_3 brick, which leads to slag penetration into MgO–Cr_2O_3 brick interior and causes a corrosion reaction between MgO and Cr_2O_3 bricks and the slag in which MgO dissolve in the slag. In Fig. 5, it also reveals that the $MgCr_2O_4$ phase causes MgO to form a discontinuous in MgO–Cr_2O_3 brick.

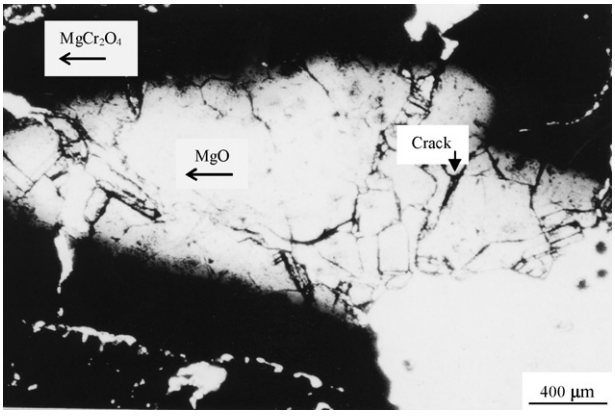

Fig. 5. The open Nicol of an optical polarized microscopy of MgO–Cr_2O_3 brick with the molten slag of MgO–Al_2O_3–SiO_2–CaO–Fe_tO at 1923 K for 8 h.

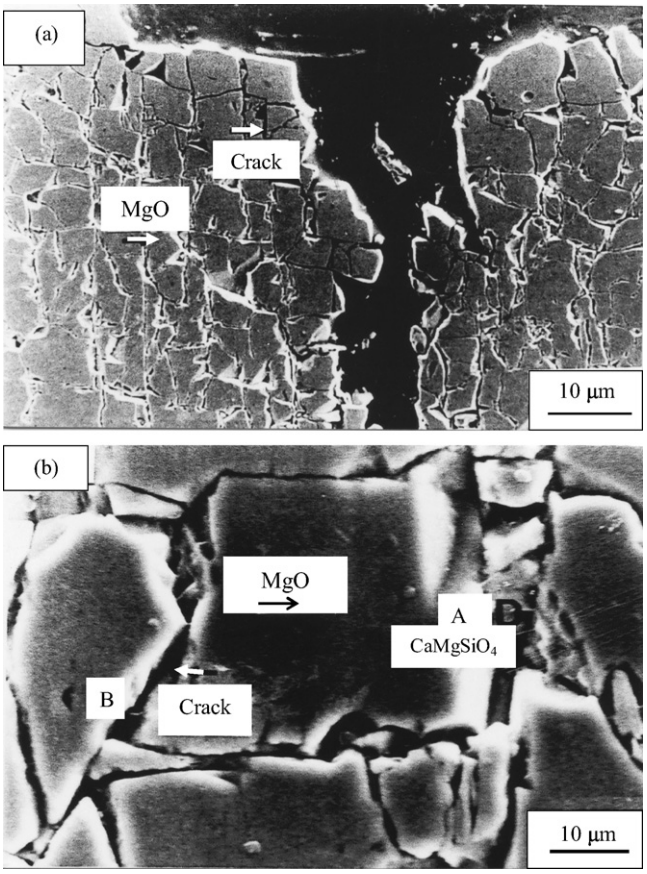

Fig. 6. (a) SEM micrograph of penetration layer of MgO–Cr_2O_3 brick reacting with molten slag at 1923 K for 4 h and (b) the enlarged view of crack in (a).

Table 6
EDS analyses of composition at different locations in Fig. 6.

Location	Composition (wt%)			
	MgO	Fe_tO	SiO_2	CaO
A	25.0	0	32.0	43.0
B	21.3	8.5	32.7	37.5

3.2. Microstructure of the MgO–Cr_2O_3 brick after the test

A SEM micrograph of the penetration layer of MgO–Cr_2O_3 brick reacting with the molten slag in an electric furnace at 1923 K for 4 h is shown in Fig. 6(a). Cracks, MgO and dissolved MgO have been identified. MgO dissolved because easily penetrated molten slag into the brick interior and reaction with it bricks, leading to a localized dissolution of MgO–Cr_2O_3 brick in the slag.

Fig. 6(b) shows the enlarged views of the crack in Fig. 6(a), which have been identified as MgO, $CaMgSiO_4$ (A) and cracks (B). The compositions of A and B in Fig. 6(b) are listed in Table 6. It have been detected that the composition of location A contains MgO, CaO, and SiO_2. According to Fig. 4, this result could be caused by the reaction of MgO with slag to form $CaMgSiO_4$ after the slag corrosion.

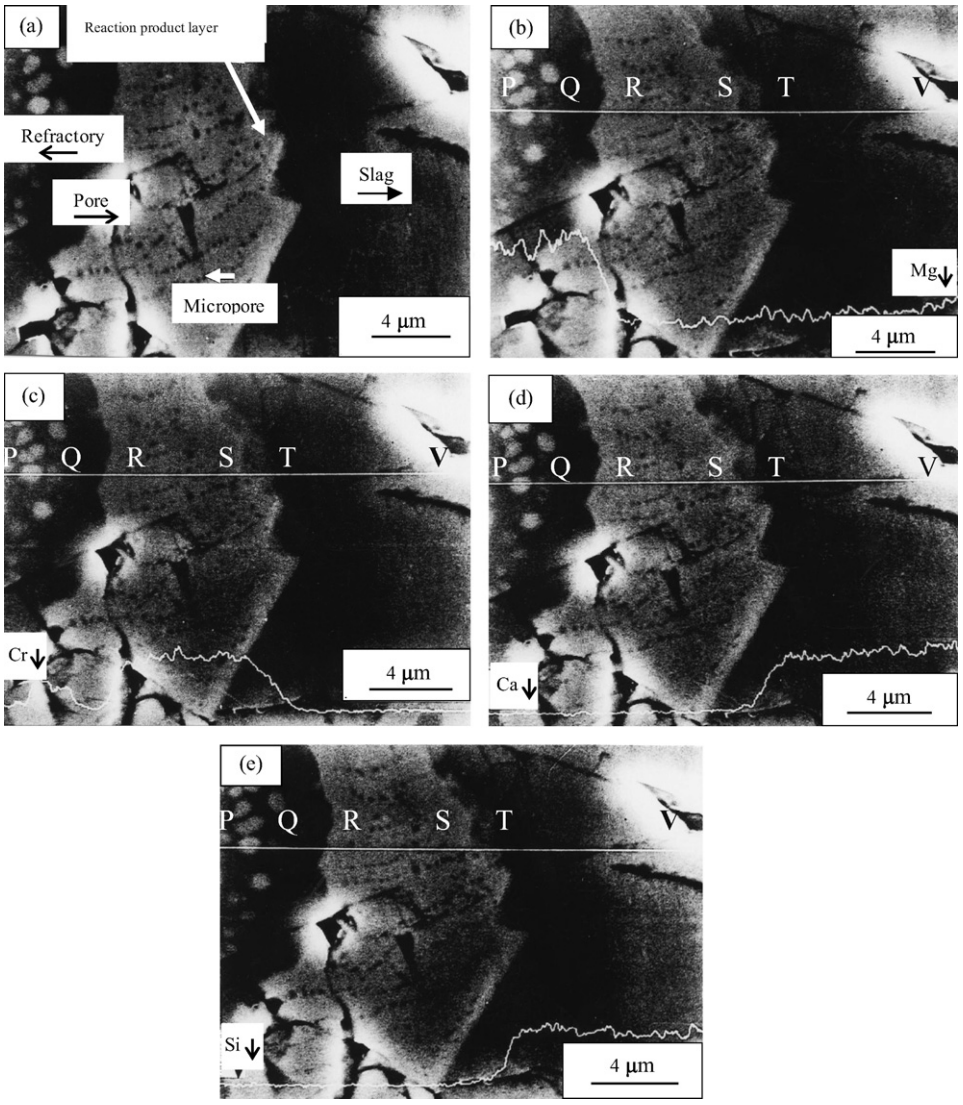

Fig. 7. SEM micrograph and line scanning of reaction product layer of $MgO–Cr_2O_3$ brick reacted with the molten slag of $MgO–Al_2O_3–SiO_2–CaO–Fe_tO$ after static slag corrosion at 1923 K for 8 h; (a) corroded surface of $MgO–Cr_2O_3$ showing MgO, $MgCr_2O_4$, pores, and the slag, (b) line scanning of MgO, (c) line scanning of Cr, (d) line scanning of Ca and (e) line scanning of Si.

A SEM micrograph and line scanning of the reaction product layer of the $MgO–Cr_2O_3$ brick after the static slag corrosion at 1923 K for 8 h are shown in Fig. 7. $MgO–Cr_2O_3$ brick, reaction product layer, pores, and slag has been identified in Fig. 7(a). In the elemental scanning of Fig. 7(b–e), there are distinct areas, namely, gray area PQ, dark area QR, light gray area RS, dark area ST, and dark and gray areas next to ST (denoted by TV). For the Mg line scanning in Fig. 7(b), the MgO content at the PR is greater than RV. However, MgO content at TV is slightly increases from RS. Table 6 indicates that the MgO content in the slag is 28.3 wt%. On the other hand, the MgO content in the $MgCr_2O_4$ is 20.9 wt%. Hence, the major crystalline phase of the PR is MgO. For the Cr line scanning in Fig. 7(c), QR has no Cr. The Cr content decreases at ST. According to Figs. 7(b) and (c), it has been identified that the major crystalline phase at RS is $MgCr_2O_4$, and ST is a reaction product layer. The width of the reaction product layer is about 2.0 μm after the test at 1923 K for 8 h. Figs. 7(d) and (e) are the line scannings of Ca and Si, respectively. The variations of Ca and Si contents are similar, and indicate that TV corresponds to is the slag. Fig. 7(b–e) show that $MgCr_2O_4$ exists at the $MgO–Cr_2O_3$ brick surface and the slag sticks to the $MgCr_2O_4$ grains, creating a reaction product layer between the $MgCr_2O_4$ and the slag.

Fig. 8 illustrates the TEM micrographs and electron diffraction (ED) patterns of the $MgO–Cr_2O_3$ brick and the $MgO–Al_2O_3–SiO_2–CaO–Fe_tO$ slag after the corrosion test at 1923 K for 4 h. Fig. 8(a) and (b) are the bright field (BF) and dark field (DF) images of the $MgCr_2O_4$ spinel and the precipitate phase of $(Mg, Fe)(Al, Cr)_2O_4$. Fig. 8(c) shows the ED patterns of the precipitate phase in the matrix of the $MgCr_2O_4$ spinel. Reflections from the precipitate and matrix are well separated and resolvable. In Fig. 8(d), the precipitate phase (small spots) is $(Mg, Fe)(Al, Cr)_2O_4$, and the matrix (open circles) is $MgCr_2O_4$.

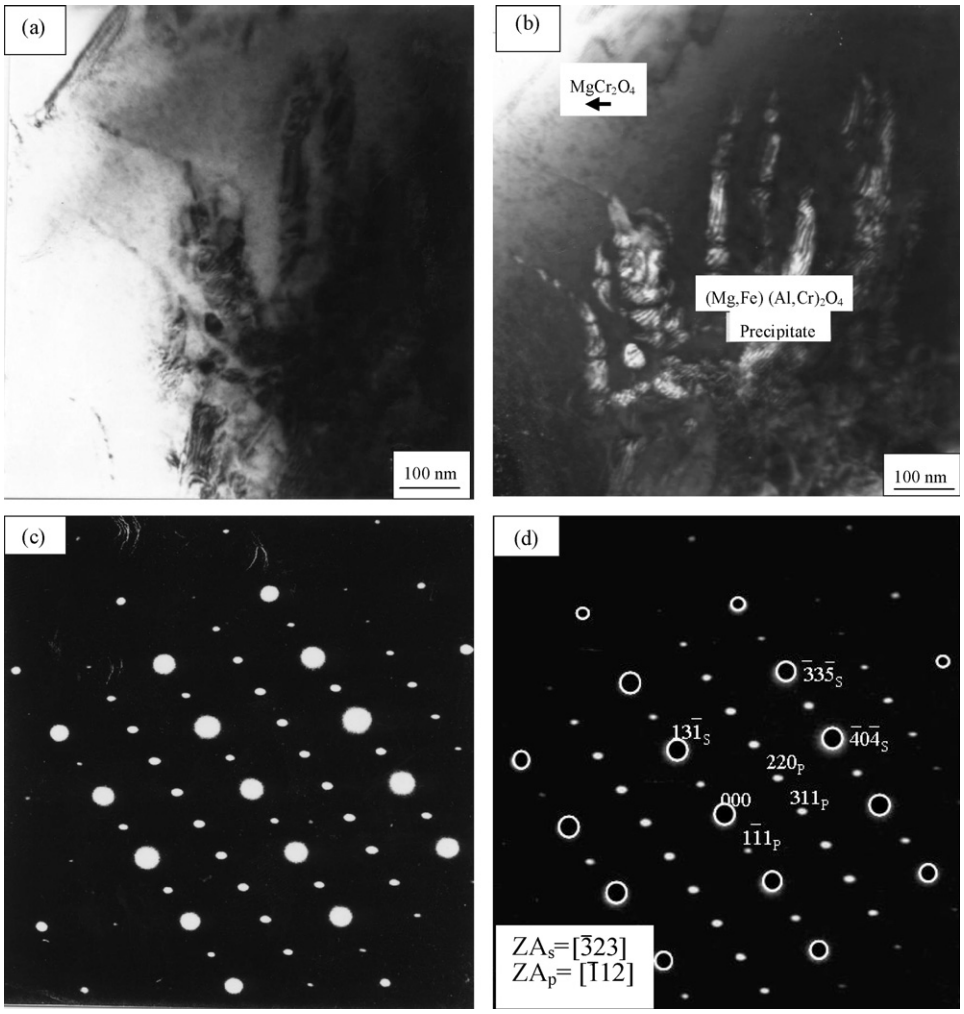

Fig. 8. TEM micrograph and ED pattern of MgO–Cr_2O_3 brick after static corrosion test at 1923 K for 4 h: (a) BF image, (b) DF image of $MgCr_2O_4$ matrix and precipitate, (c) ED pattern of $MgCr_2O_4$ and (Mg, Fe)(Al, Cr_2)O_4, and (d) indexed ED pattern, showing matrix pattern indexed as $MgCr_2O_4$ spinel (open circle, denoted by S, A_s = [323]) and (Mg, Fe)(Al, Cr)$_2O_4$ (small spots, denoted by P, ZA_p = [112]).

4. Conclusions

The reaction between the MgO–Cr_2O_3 brick and the molten slag of MgO–Al_2O_3–SiO_2–CaO–Fe_tO after static slag corrosion test at 1823–1923 K for 2–8 h and the resulting microstructure have been investigated. The results of this study are summarized as follows:

1. The MgO–Cr_2O_3 brick reacts with the molten slag of MgO–Al_2O_3–SiO_2–CaO–Fe_tO in the static slag corrosion at 1923 K for 4 h. The XRD results show that the mirror phases of the brick are MgO periclase and $MgCr_2O_4$ spinel with $CaMgSiO_4$ as the minor phase.
2. SEM results show that the $MgCr_2O_4$ spinel exists at the MgO–Cr_2O_3 brick surface. The slag sticks to $MgCr_2O_4$ grains, creating a reaction product layer between $MgCr_2O_4$ and the slag.
3. TEM micrographs and ED patterns demonstrate that the minor phase of (Mg, Fe)(Al, Cr)$_2O_4$ precipitates in the $MgCr_2O_4$ matrix.

Acknowledgements

This work was supported by the Ministry of Economic Affairs of Taiwan, and China Steel Corporation under Contract No. 87R13, and the National Science Council of Taiwan, under Contract No. NSC84-2216-E-151-005. We also sincerely thank Prof. M.P. Hung for extensive manuscript revision.

References

[1] M. Baba, Current status of JISF'S iron ore smelting reduction process, Trans. Instn. Min. Metall. 103 (1994) C15–20.
[2] M.L. Keith, Phase equilibria in the system MgO–Cr_2O_3–SiO_2, J. Am. Ceram. Soc. 37 (10) (1954) 490–496.
[3] E.P. Glasser, E.F. Osbron, Phase equilibrium studies in the system CaO–Cr_2O_3–SiO_2, J. Am. Ceram. Soc. 41 (9) (1958) 358–367.
[4] E.P. Glasser, E.F. Osbron, Phase of diagrams of ceramist, Am. Ceram. Soc. 1 (1964) 226.
[5] K. Morita, T. Shibuya, N. Sano, The solubility of the chromite in MgO–Al_2O_3–SiO_2–CaO melts at 1600 °C in air, Tetsu to Hagane 70 (4) (1988) 632–639.

[6] K. Ichikawa, R. Nakamura, M. Ogata, M. Suto, Distribution and properties of secondary spinel in magnesia–chrome bricks, Shimagawa Technical Report 39 (1996) 25–34.
[7] T. Takahashi, New smelting process and refractories, Tetsu to Hagane 80 (6) (1994) 440–445.
[8] Z. Tao, K. Mukai, S. Yoshinaga, M. Ogata, Corrosion of magnesia–chrome refractory with molten slag for DIOS, Taikabutsu Jpn. 50 (6) (1998) 316–325.
[9] Z. Tao, K. Mukai, M. Ogata, Local corrosion of magnesia–chrome refractory at slag–metal interface, Taikabutsu Overseas 19 (2) (1999) 3–10.
[10] W.E. Lee, R.E. Moore, Evolution of in situ refractories in the 20th century, J. Am. Ceram. Soc. 81 (6) (1998) 1385–1410.
[11] J.M. Robin, Y. Berthaud, N. Schmitt, J. Poirier, D. Thermines, Thermo-mechanical behaviour of magnesia–carbon refractories, Brit. Ceram. Trans. 97 (1) (1998) 1–10.